Anisotropic effective permittivity of an ultrathin gold coating on optical fiber in air, water and saline solutions

Wenjun Zhou,[1,*] David J. Mandia,[2] Seán T. Barry,[2] and Jacques Albert[1]

[1]*Department of Electronics, Carleton University, Ottawa, ON K1S 5B6, Canada*
[2]*Department of Chemistry, Carleton University, Ottawa, ON K1S 5B6, Canada*
[*]*wenjun.zhou@carleton.ca*

Abstract: The optical properties of an ultrathin discontinuous gold film in different dielectric surroundings are investigated experimentally by measuring the polarization-dependent wavelength shifts and amplitudes of the cladding mode resonances of a tilted fiber Bragg grating. The gold film was prepared by electron-beam evaporation and had an average thickness of 5.5 nm (± 1 nm). Scanning electron imaging was used to determine that the film is actually formed of individual particles with average lateral dimensions of 28 nm (± 8 nm). The complex refractive indices of the equivalent uniform film in air at a wavelength of 1570 nm were calculated from the measurements to be 4.84–i0.74 and 3.97–i0.85 for TM and TE polarizations respectively (compared to the value for bulk gold: 0.54-i10.9). Additionally, changes in the birefringence and dichroism of the films were measured as a function of the surrounding medium, in air, water and a saturated NaCl (salt) solution. These results show that the film has stronger dielectric behavior for TM light than for TE, a trend that increases with increasing surrounding index. Finally, the experimental results are compared to predictions from two widely used effective medium approximations, the generalized Maxwell-Garnett and Bruggeman theories for gold particles in a surrounding matrix. It is found that both of these methods fail to predict the observed behavior for the film considered.

OCIS codes: (060.3735) Fiber Bragg gratings; (310.6860) Thin films, optical properties; (160.3900) Metals; (160.4236) Nanomaterials.

References and links

1. U. Kreibig and M. Vollmer, *Optical Properties of Metal Clusters* (Springer, 1995), Chap. 4.1.2.
2. J. J. Tu, C. C. Homes, and M. Strongin, "Optical properties of ultrathin films: evidence for a dielectric anomaly at the insulator-to-metal transition," Phys. Rev. Lett. **90**(1), 017402 (2003).
3. M. Hövel, B. Gompf, and M. Dressel, "Dielectric properties of ultrathin metal films around the percolation threshold," Phys. Rev. B **81**(3), 035402 (2010).
4. M. Svedendahl, P. Johansson, and M. Käll, "Complete light annihilation in an ultrathin layer of gold nanoparticles," Nano Lett. **13**(7), 3053–3058 (2013).
5. M. Yan, J. Dai, and M. Qiu, "Lithography-free broadband visible light absorber based on a mono-layer of gold nanoparticles," J. Opt. **16**(2), 025002 (2014).
6. N. Liu, M. Mesch, T. Weiss, M. Hentschel, and H. Giessen, "Infrared perfect absorber and its application as plasmonic sensor," Nano Lett. **10**(7), 2342–2348 (2010).
7. A. Manjavacas and F. J. García de Abajo, "Tunable plasmons in atomically thin gold nanodisks," Nat Commun **5**, 3548 (2014).
8. A. Sihvola, *Electromagnetic Mixing Formulas and Applications* (The Institution of Electrical Engineers, 1999), Chap. 9.
9. H. T. Beyene, J. W. Weber, M. A. Verheijen, M. C. M. van de Sanden, and M. Creatore, "Real time in situ spectroscopic ellipsometry of the growth and plasmonic properties of Au nanoparticles on SiO_2," Nano Res. **5**(8), 513–520 (2012).

#225262 - $15.00 USD Received 20 Oct 2014; revised 3 Dec 2014; accepted 4 Dec 2014; published 15 Dec 2014

10. X. D. Li, T. P. Chen, Y. Liu, and K. C. Leong, "Influence of localized surface plasmon resonance and free electrons on the optical properties of ultrathin Au films: a study of the aggregation effect," Opt. Express **22**(5), 5124–5132 (2014).
11. Y. Battie, A. E. Naciri, W. Chamorro, and D. Horwat, "Generalized effective medium theory to extract the optical properties of two-dimensional nonspherical metallic nanoparticle layers," J. Phys. Chem. C **118**(9), 4899–4905 (2014).
12. T. Ung, L. M. Liz-Marzán, and P. Mulvaney, "Optical properties of thin films of Au@SiO_2 particles," J. Phys. Chem. B **105**(17), 3441–3452 (2001).
13. J. Toudert, L. Simonot, S. Camelio, and D. Babonneau, "Advanced optical effective medium modeling for a single layer of polydisperse ellipsoidal nanoparticles embedded in a homogeneous dielectric medium: surface plasmon resonances," Phys. Rev. B **86**(4), 045415 (2012).
14. W.-J. Lee, J.-E. Kim, H.-Y. Park, S. Park, M.-S. Kim, J. T. Kim, and J. J. Ju, "Optical constants of evaporated gold films measured by surface plasmon resonance at telecommunication wavelengths," J. Appl. Phys. **103**(7), 073713 (2008).
15. X. Wang, K.-P. Chen, M. Zhao, and D. D. Nolte, "Refractive index and dielectric constant transition of ultra-thin gold from cluster to films," Opt. Express **18**(24), 24859–24867 (2010).
16. J. Albert, L.-Y. Shao, and C. Caucheteur, "Tilted fiber Bragg grating sensors," Laser Photonics Rev. **7**(1), 83–108 (2013).
17. M. Z. Alam and J. Albert, "Selective excitation of radically and azimuthally polarized optical fiber cladding modes," J. Lightwave Technol. **31**(19), 3167–3175 (2013).
18. W. Zhou, D. J. Mandia, M. B. E. Griffiths, A. Bialiayeu, Y. Zhang, P. G. Gordon, S. T. Barry, and J. Albert, "Polarization-dependent properties of the cladding modes of a single mode fiber covered with gold nanoparticles," Opt. Express **21**(1), 245–255 (2013).
19. C. Caucheteur, C. Chen, V. Voisin, P. Berini, and J. Albert, "A thin metal sheath lifts the EH to HE degeneracy in the cladding mode refractometric sensitivity of optical fiber sensors," Appl. Phys. Lett. **99**(4), 041118 (2011).
20. Y.-C. Lu, R. Geng, C. Wang, F. Zhang, C. Liu, T. Ning, and S. Jian, "Polarization effects in tilted fiber Bragg grating refractometers," J. Lightwave Technol. **28**(11), 1677–1684 (2010).
21. Y. Y. Shevchenko and J. Albert, "Plasmon resonances in Gold-coated tilted fiber Bragg gratings," Opt. Lett. **32**(3), 211–213 (2007).
22. Y. Shevchenko, C. Chen, M. A. Dakka, and J. Albert, "Polarization-selective grating excitation of plasmons in cylindrical optical fibers," Opt. Lett. **35**(5), 637–639 (2010).
23. J.-M. Renoirt, M. Debliquy, J. Albert, A. Ianoul, and C. Caucheteur, "Surface plasmon resonances in oriented silver nanwire coatings on optical fibers," J. Phys. Chem. C **118**(20), 11035–11042 (2014).
24. W. Zhou, D. J. Mandia, M. B. E. Griffiths, S. T. Barry, and J. Albert, "Effective permittivity of ultrathin chemical vapor deposited gold films on optical fibers at infrared wavelengths," J. Phys. Chem. C **118**(1), 670–678 (2014).
25. L.-Y. Shao, J. P. Coyle, S. T. Barry, and J. Albert, "Anomalous Permittivity and Plasmon Resonances of Copper Nanoparticle Conformal Coatings on Optical Fibers," Opt. Mater. Express **1**(2), 128–137 (2011).
26. I. Horcas, R. Fernández, J. M. Gómez-Rodríguez, J. Colchero, J. Gómez-Herrero, and A. M. Baro, "WSXM: A software for scanning probe microscopy and a tool for nanotechnology," Rev. Sci. Instrum. **78**(1), 013705 (2007).
27. S. Kedenburg, M. Vieweg, T. Gissibl, and H. Giessen, "Linear refractive index and absorption measurements of nonlinear optical liquids in the visible and near-infrared spectral region," Opt. Mater. Express **2**(11), 1588–1611 (2012).
28. J. Lin and C. W. Brown, "Near-IR spectroscopic determination of NaCl in aqueous solution," Appl. Spectrosc. **46**(12), 1809–1815 (1992).
29. A. Yariv and P. Yeh, *Photonics: Optical Electronics in Modern Communications, 6th ed.* (Oxford University Press, 2007), Chap. 3.2.
30. P. B. Johnson and R. W. Christy, "Optical constants of the noble metals," Phys. Rev. B **6**(12), 4370–4379 (1972).
31. A. Kossoy, V. Merk, D. Simakov, and K. Leosson, "Optical and structural properties of ultra-thin gold films," Adv. Opt. Mater. (to be published), doi:10.1002/adom.201400345.
32. S. Laref, J. Cao, A. Asaduzzaman, K. Runge, P. Deymier, R. W. Ziolkowski, M. Miyawaki, and K. Muralidharan, "Size-dependent permittivity and intrinsic optical anisotropy of nanometric gold thin films: a density functional theory study," Opt. Express **21**(10), 11827–11838 (2013).
33. S. D. Campbell, R. W. Ziolkowski, J. Cao, S. Laref, K. Muralidharan, and P. Deymier, "Anisotropic permittivity of ultra-thin crystalline Au films: Impacts on the plasmonic response of metasurfaces," Appl. Phys. Lett. **103**(9), 091106 (2013).
34. J. C. Maxwell Garnett, "Colours in metal glasses and in metallic films," Philos. Trans. R. Soc. Lond. A **203**(359-371), 385–420 (1904).
35. D. A. G. Bruggeman, "Berechnung verschiedener physikalischer Konstanten von heterogenen Substanzen. I. Dielektrizitätskonstanten und Leitfähigkeiten der Mischkörper aus isotropen Substanzen," Ann. Phys. **416**(7), 636–664 (1935).

#225262 - $15.00 USD Received 20 Oct 2014; revised 3 Dec 2014; accepted 4 Dec 2014; published 15 Dec 2014

36. S. B. Jones and S. P. Friedman, "Particle shape effects on the effective permittivity of anisotropic or isotropic media consisting of aligned or randomly oriented ellipsoidal particles," Water Resour. Res. **36**(10), 2821–2833 (2000).
37. R. W. Cohen, G. D. Cody, M. D. Coutts, and B. Abeles, "Optical properties of granular silver and gold films," Phys. Rev. B **8**(8), 3689–3701 (1973).
38. U. Kreibig and M. Vollmer, *Optical Properties of Metal Clusters* (Springer, 1995), Chap. 4.4.
39. M. Walther, D. G. Cooke, C. Sherstan, M. Hajar, M. R. Freeman, and F. A. Hegmann, "Terahertz conductivity of thin gold films at the metal-insulator percolation transition," Phys. Rev. B **76**(12), 125408 (2007).
40. Y. Yagil, P. Gadenne, C. Julien, and G. Deutscher, "Optical properties of thin semicontinuous gold films over a wavelength range of 2.5 to 500 μm," Phys. Rev. B **46**(4), 2503–2511 (1992).

1. Introduction

Ultrathin gold films with thicknesses under 10 nm show size- and geometry-dependent features in their optical and plasmonic properties that are quite different from those of bulk material [1]. With decreasing thickness the thin gold films evolve morphologically from continuous to granular, during which a metal-to-insulator transition occurs [2,3]. The ultrathin gold aggregates can be represented by a single layer of oblate nanoparticles (NPs), and such layers have important applications as selective light absorbers [4,5] and many kinds of plasmonic devices [6,7]. Using the effective medium approximation (EMA) theories of the early 1900s [8], the complex effective permittivity of the aggregated gold films embedded in a homogeneous matrix (surrounding material) can be simulated. In the EMA models, the gold aggregates are represented by point dipoles embedded in the homogenous background, and the resulting effective permittivity of the mixture is dependent on the complex permittivities of the two constituents (gold and surrounding material), and on the volume fraction of gold. For experimental studies of thin gold films, spectroscopic ellipsometry is one of the most common measurement tools as it is highly sensitive to the optical properties of thin films [3], [9–11]. However, most of the previous work in this area was focused on measuring the thickness-dependent complex permittivity calculated from the ellipsometric angles to investigate the effect of various thin film growth mechanisms, including the impact of the shape and distribution of the NPs making up the ultrathin films. Comparatively few studies exist on the impact of the surrounding medium permittivity of these films [12,13], and in such cases the gold NPs films are always embedded in solid dielectric material, making it impossible to study the same film under different surroundings. Moreover, the anisotropic optical properties of the ultrathin metal films caused by the nonspherical shape of their NP constituents limit the measurement accuracy of the conventional measurement methods, such as spectral reflectometry [3,14], ellipsometry [9,10], and interferometric picometrology [15]. This is one of the reasons for which previous works often neglected the optical anisotropy in measurements of gold films with thicknesses spanning the insulator-to-metal transition. The purpose of the present paper is to investigate the impact of the surrounding medium on the anisotropic optical properties of highly disordered, morphologically complex gold NP aggregates with an average thickness of 5.5 nm. This experimental study is carried out by probing the ultrathin film, deposited on the surface of the cladding of an optical fiber by two-step evaporation, using the polarized evanescent fields of the fiber cladding modes that are resonantly excited by a tilted fiber Bragg grating (TFBG) [16,17]. The anisotropic properties of the thin film are inferred from the changes in the amplitudes and wavelengths of the various cladding modes as the film coated fiber is exposed to various surroundings. Those results are then compared with EMA calculations based on measured NP shapes and bulk values of their permittivities, and the discrepancies observed are discussed in relation with the assumptions made by both the Maxwell-Garnett (M-G) and Bruggeman EMA models.

#225262 - $15.00 USD Received 20 Oct 2014; revised 3 Dec 2014; accepted 4 Dec 2014; published 15 Dec 2014

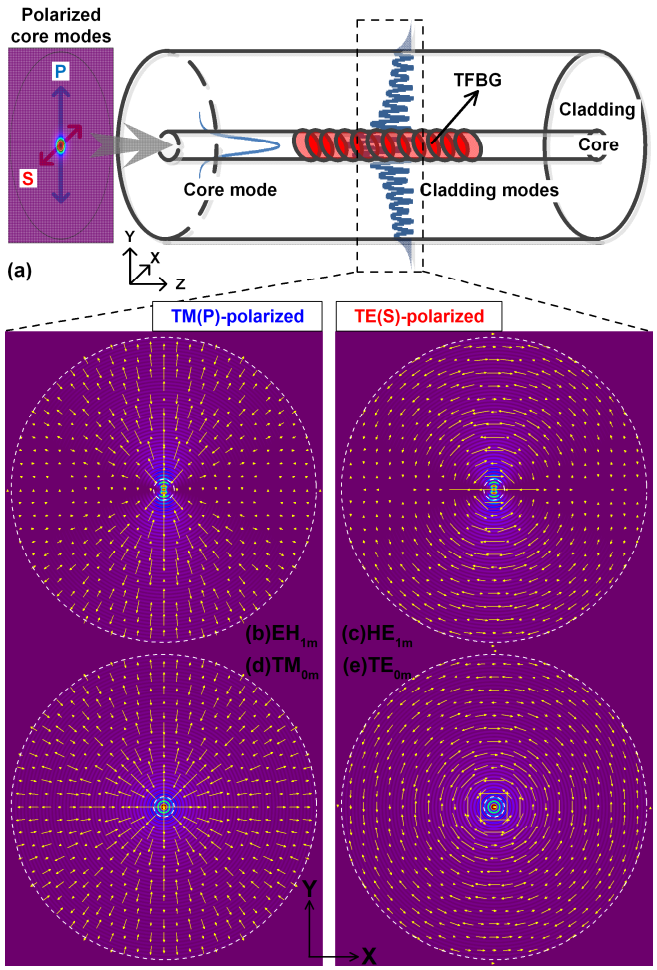

Fig. 1. (a) Schematic diagram of TFBG under X-(S-) and Y-(P-) polarized core modes input. Electric field distributions of four typically vectorial cladding modes ((b) EH_{1m}, (c) HE_{1m}, (d) TM_{0m}, and (e) TE_{0m}) coupled from the X-(S-) and Y-(P-) polarized core modes by TFBG, respectively. (Note that the grating planes are parallel to X axis and tilted away from the Y axis). The white broken curves indicate the core and cladding edges of optical fiber.

In more detail, due to the inclination of the grating planes of a TFBG along a specific direction, two families of polarized cladding modes with radial or azimuthal electric fields at the fiber cladding boundary can be selectively excited by probing with linearly polarized input core-guided light (as shown in Fig. 1) [16,17]. Figures 1(b), 1(c), 1(d), and 1(d) illustrate the simulated electric fields of four typical polarized cladding modes with the same radial order (number of zeros in field amplitude as a function of radial coordinate) in standard single mode fiber for telecommunications. TM_{0m} and EH_{nm} modes are radially polarized and result from P-polarized core mode input while the TE_{0m} and HE_{nm} modes are azimuthally polarized and result from S-polarized input. P- and S-polarizations refer to the orientation of the input electric field in the plane of incidence and out of the plane of incidence on the tilted grating fringes, respectively. In the following these mode families will be referred to as TM and TE to shorten the text. Due to the orthogonal electric fields at the interface of fiber cladding and surroundings, the TM- and TE-polarized cladding modes show distinct responses to surrounding refractive index (SRI) changes, but more strongly so when metal coatings or particles are present [18]- [20]. Therefore, the polarization-dependent properties of the cladding modes excited by TFBG can be used for surface plasmon resonance sensors [21–23]

#225262 - $15.00 USD Received 20 Oct 2014; revised 3 Dec 2014; accepted 4 Dec 2014; published 15 Dec 2014

and measuring the anisotropic optical properties of thin metal coatings [24,25]. In this paper, the SRI-dependent spectral responses of the two kinds of polarized cladding modes are used to investigate the effect of the surrounding permittivity on the anisotropic effective optical properties of an ultrathin gold NP film with a mean thickness of 5.5 nm. Since the coated TFBG is both the substrate for the coating and the probe of its properties, successive measurements of a given coating in many surrounding environments can be very accurate as they are inherently independent of changes in either the film or the sensing probes, which remain unchanged. The complex effective permittivities of the coating are measured and compared with theoretical predictions based on both the generalized M-G and Bruggeman EMAs, wherein the input parameters are particle sizes and filling factors, extracted from scanning electron microscope (SEM) and atomic force microscope (AFM) image data, as well as literature values for the permittivity of bulk gold and of the surrounding media tested.

2. Sample fabrication and geometry

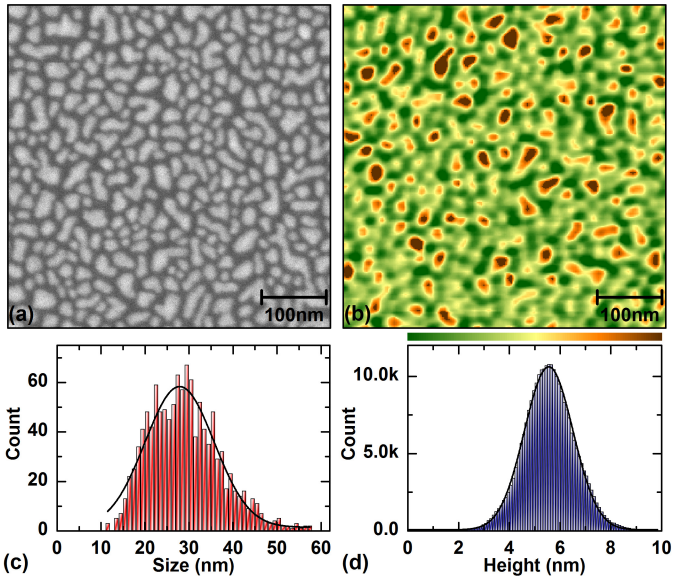

Fig. 2. SEM (a) and AFM (b) images of the gold NPs film over an area of 0.5 × 0.5 μm^2 (with scale bar of 100 nm). (c) Histogram of gold NP lateral sizes based on 1172 particles distributed over an area of approximately 1.3 × 1.0 μm^2. (d) Height histogram of gold NPs film based on ~2.62 × 10^5 extracted points from 1 × 1 μm^2 AFM image.

The TFBG used in this work was written in hydrogen-loaded CORNING SMF-28 fiber with a pulsed KrF excimer laser using the phase-mask method [16]. The hydrogenation process of the optical fibers is as follows: a pressure of 15.2 MPa, a temperature of 20 °C, and a duration of 14 days. The length and the tilt angle were chosen at 10 mm and 10° to excite a large number of high-order cladding modes with strong evanescent fields for thin coating measurements. The Bragg wavelength is around 1613 nm, resulting from a phase mask period of 1114.8 nm. After cleaning the TFBG cladding surface with piranha solution (a mixture of sulfuric acid and hydrogen peroxide), it was placed in an electron-beam physical vapor deposition system at room temperature and under vacuum (10^{-6} Torr). In order to have a relatively uniform gold coating around the fiber circumference, two gold deposition steps were conducted consecutively with the fiber being rotated by exactly 180° between the two deposition runs using a custom designed fiber holding fixture. A relatively uniform gold film with a thickness of ~5 nm was obtained under a deposition rate of ~6 nm/min. The estimated thickness was obtained by measuring a witness sample (a 2-inch silicon wafer with a 30 nm SiO_2 thermal oxide buffer layer) that was placed next to the TFBG for one deposition run. We

#225262 - $15.00 USD Received 20 Oct 2014; revised 3 Dec 2014; accepted 4 Dec 2014; published 15 Dec 2014

now proceed to describe physical measurements of the actual coating morphology (thickness and NP shapes and filling factor) on the witness sample.

Figure 2 shows SEM (a) and AFM (b) images which show that the SiO_2 surface is completely covered by an irregular distribution of gold NPs. The evidence of small-scale coalescence of the aggregated gold NPs is already appearing for this thickness, resulting from the touching and merging of adjacent NPs. The quantitative analysis of the gold NP sizes and heights was carried out on the SEM and AFM images by using image processing software tools ImageJ and WSxM [26], respectively. The distributions of the lateral size (diameter) and height of the gold NPs film are shown in Figs. 2(c) and 2(d), respectively. Based on the Gaussian fitting curves, the mean lateral size d_{NP} and height h_{NP} of the gold NPs are 28 nm with a standard deviation of 8 nm and 5.5 nm with a standard deviation of 1 nm, respectively. The relatively large standard deviations in lateral size and height reflect the randomness of the cluster formation at these thicknesses, as can be clearly observed in Figs. 2(a) and 2(b). It is very clear that this 5.5 nm thick gold evaporated film can be regarded as a mono-layer of oblate gold nanospheroids. Also, the volume factor f of the gold NPs is 68% (± 5%), as obtained from the SEM image using the ImageJ software.

3. Experimental results

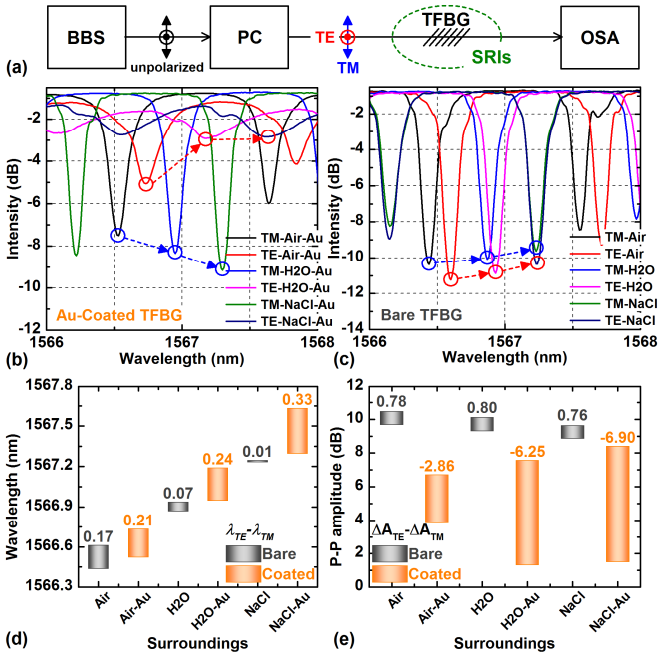

Fig. 3. (a) Schematic diagram of experimental setup. Temperature-calibrated spectra of the gold NPs-coated (b) and the gold NPs-etched (bare) (c) TFBGs for TE- and TM-polarizations in air, DI water (H_2O), and saturated NaCl-water solution (NaCl) surroundings. (The red and blue circles are marked at the positions of the TE- and TM-polarized cladding mode resonances, respectively.) Wavelength separations (d) and peak-to-peak amplitude differences (e) between the pair of polarized cladding modes for the both of coated and bare TFBGs under the three SRIs. Note that the signs of the P-P amplitude differences under the cases of bare and coated TFBGs are opposite.

Based on the experimental setup shown in Fig. 3(a) that includes a broadband source (BBS) (JDSU BBS1560), a polarization controller (PC) (JDSU PR2000), and an optical spectrum analyzer (OSA) (ANDO AQ6317B), the polarized spectra of TFBG under various SRIs can be measured [24]. Even though the nominal measurement resolution of this OSA is only 10 pm, the resonance lineshapes were fitted with an inverted Gaussian function over several

#225262 - $15.00 USD Received 20 Oct 2014; revised 3 Dec 2014; accepted 4 Dec 2014; published 15 Dec 2014

measurement points and the statistically significant uncertainty with which an individual resonance can be measured is ± 2 pm for the wavelength and ± 0.05 dB for the amplitude [16]. In this experiment, three different SRIs of 1, 1.315–i1.21 × 10^{-4} [27], and 1.360–i3.24 × 10^{-5} [28] (at 1570 nm) provided by air, deionized water, and a saturated NaCl-water solution were applied on the TFBG sample. In order to investigate the coating with the same cladding guided mode (resonance) in the three different SRIs, a resonance near 1566.5 nm (measured in air) was chosen, as the cut-off wavelength for cladding mode guidance in the largest SRI is around 1565 nm. The normalized spectra of the polarized cladding modes of the gold NPs-coated TFBG under the three surroundings is shown in Fig. 3(b). The spectra were adjusted to compensate for any temperature dependence by shifting them so that the core mode resonances for all the measurements (located near 1613 nm) overlap perfectly [16]. All the spectra shown in Fig. 3 were obtained with the same TFBG, to eliminate any possible perturbation of the data by different underlying grating properties (it is not possible to fabricate exactly identical TFBGs by photosensitive processes). For comparison with the gold coated results, corresponding spectra of the same TFBG sample after etching of the gold coating are shown in Fig. 3(c). In Figs. 3(d) and 3(e), the floating columns indicate the extracted wavelength separations (λ_{TE}–λ_{TM}) and peak-to-peak (P-P) amplitude differences (ΔA_{TE}–ΔA_{TM}) between the TE- and TM-polarized cladding mode resonances under the three SRIs for both bare and coated TFBG samples.

It is obvious that the TE and TM cladding mode resonances both shift to longer wavelength under increasing SRI, as expected from standard waveguide theory, and roughly at the same average rate under these conditions (Fig. 3(d)). Also as expected, the wavelength difference between TE and TM resonances of the bare grating decreases from 0.173 nm to 0.013 nm with increasing SRI, indicating that the modes chosen approach their cut-off at the maximum SRI tested (since weakly guided and radiation modes no longer have polarization splitting [20]). For the gold coated TFBG on the other hand the SRI dependence of the wavelength shifts completely opposite: the wavelength separation for the same pair of resonances is larger in air (0.210 vs 0.173 nm) and it further increases to 0.335 nm under the same changes of SRI as for the bare grating. So instead of reducing the polarization splitting, increasing the SRI makes the splitting larger when the TFBG is coated with the thin gold NP film.

With regards to the amplitudes of the resonances as the SRI rises, they decrease slowly for the bare TFBG as the modes approach cut off, and the amplitudes of the TM modes are slightly lower, due to the weaker confinement of those modes relative to the TE ones. Again the results for the grating with the gold coating are strikingly different. For the coated grating in air, the P-P amplitudes of all the modes are smaller than those of the bare grating, reflecting higher mode loss due to either absorption or scattering by the gold NPs. Upon increasing the SRI however, the amplitudes of the TM modes recover (they become larger, indicating lower mode loss) while those of TE modes continue to decrease. In fact, the overall spectral responses of the coated TE and TM modes indicate clearly that for such gold coatings, TE modes (with their electric fields polarized parallel to the film) are much more perturbed and are also more sensitive to further SRI changes.

4. Discussions

In order to investigate the anisotropic optical properties of the gold NPs coating under the various SRIs, the effective indices of the polarized cladding modes have to be extracted from the spectral data. Then, those mode effective indices (along with the average coating thickness obtained by AFM) will be used to calculate the effective medium properties of the equivalent homogeneous layer that is added to the fiber waveguiding structure by the coating process. Figure 4 illustrates the evanescent fields of the cladding modes with TE- or TM-polarization along the gold NPs-coated TFBG surface (a) and the corresponding waveguide (b) where the NPs have been replaced by an effective medium layer with homogeneous properties. Since

#225262 - $15.00 USD Received 20 Oct 2014; revised 3 Dec 2014; accepted 4 Dec 2014; published 15 Dec 2014

the added layer has a complex permittivity, its effect on the effective indices of the TE and TM cladding modes is widely different [18,21–24].

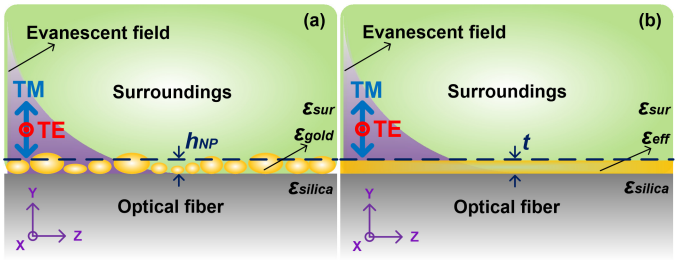

Fig. 4. 2D schematic diagrams of a mono-layer of oblate gold NPs (a) and effective medium layer that consists of gold and surrounding materials (b) coated on optical fiber surface under evanescent fields of TE- and TM-polarized cladding modes propagating along the z-axis. The thickness t of the effective medium layer is equal to the average height h_{NP} of the gold NP film measured from its AFM image. Note that the relative profiles of evanescent field and gold film shown above are not to scale, since the penetration depth of the cladding mode with effective index of ~1.366 in air is about 130 nm.

The real part of the effective index of a cladding mode N_{eff}^{clad} can be obtained from the phase matching condition of the TFBG,

$$N_{eff}^{clad} = \lambda_{clad} \cos\theta / \Lambda - N_{eff}^{core} \tag{1}$$

where λ_{clad} is the wavelength of the cladding mode resonance, θ is the tilt angle of the grating planes, Λ is the grating period, and N_{eff}^{core} is the effective index of the core mode (~1.447). The formula relating the imaginary part K_{eff}^{clad} (the mode extinction coefficient) to the amplitude of the cladding mode attenuation in the transmission spectrum requires the computation of the coupling coefficient κ between the incident core mode and the cladding mode of interest, given the known grating length and period, and the base fiber properties. The fundamental relationship between the coupling coefficient κ and the P-P transmission amplitude ΔA (converted from dB to linear scale) of the cladding mode can be written as,

$$\kappa = \frac{\tanh^{-1}\sqrt{1-\Delta A}}{L} \tag{2}$$

where L is the grating length (10 mm). This relationship is correct for the lossless case (no gold film). Once loss is introduced (the film), the coupling coefficient is unchanged to first order and the observed decrease in the P-P amplitude is due to the appearance of an imaginary part (i.e. absorption) in the cladding mode propagation constant. This imaginary part is found by matching experimental results to simulations of TFBGs with lossy modes, carried out with a numerical tool (Optigrating, by Optiwave) [24,25]. Figures 5(a) and 5(b) show the real and imaginary parts of complex effective indices for TE and TM modes of the gold coated fiber extracted from the experimental mode resonances when the coated fiber was immersed in the three SRIs (Fig. 3(b)). The real part of the effective indices increases with SRI and the difference (TE-TM) increases from 0.00038 to 0.0006. On the other hand, the calculation of the imaginary part of the effective index reveals that the extinction coefficient of the TE mode is enhanced from 1.51×10^{-4} to 5.06×10^{-4} in going from air to water, but decreases to 4.12×10^{-4} in the salt-water solution. For the TM mode, extinction coefficient drops from 4.43×10^{-5} in air to 7×10^{-6} in the salt-water solution. It is important to note that the extinction coefficient for both TE and TM modes of the bare TFBG in the salt water solution is about 1×10^{-6}, which indicates absorption in the surrounding medium (due to its bulk extinction

#225262 - $15.00 USD Received 20 Oct 2014; revised 3 Dec 2014; accepted 4 Dec 2014; published 15 Dec 2014

coefficient of 3.24 × 10^{-5}) contributes little to the extinction coefficient of the modes of the coated fiber.

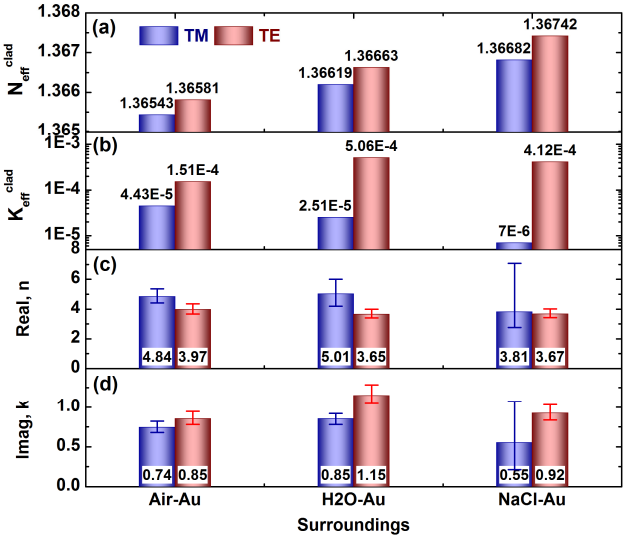

Fig. 5. Real (a) and imaginary (b) parts of the complex effective indices of the TE and TM cladding modes ($N_{eff}^{clad} - iK_{eff}^{clad}$) under the three SRIs; Real (c) and imaginary (d) parts of complex refractive indices (n – ik) of the 5.5 nm thick effective homogeneous gold NPs film for TE and TM modes. The positive and negative errors of the complex refractive indices are evaluated from the thickness uncertainty of ± 1 nm in FIMMWAVE simulations.

Now using the same optical fiber parameters (core and cladding) as those used in our previous paper [24], a thickness of 5.5 nm for the effective medium layer and the different SRIs as the outer layer, a four-layer optical fiber model solved with a vectorial finite differences method (FDM) complex mode solver (FIMMWAVE, by Photon Design) can be used to find the complex refractive index of the gold NP film (n–ik) that reproduces the measured mode effective indices [24,25]. While TE and TM modes always have different effective indices even for homogeneous, isotropic media [29], in the present case it was not possible to find a unique value of the complex film refractive index to yield the measured TE and TM modes: a film anisotropy had to be introduced to account for in-plane (TE) and out-of-plane (TM) electric field polarizations. The calculated effective medium complex refractive indices of the gold NPs film under the three SRIs at the cladding mode wavelength around 1570 nm are shown in Figs. 5(c) and 5(d). The different real and imaginary parts of the refractive indices for the TE and TM polarizations under the various surroundings indicate that the 5.5 nm gold NP film is optically anisotropic at this near infrared wavelength. Furthermore, the SRI dependence of complex refractive indices demonstrate that the gold NPs coating on TFBG surface can be regarded as a composite material layer consisting of gold NPs and a given surrounding medium. Compared with the complex refractive index of bulk gold (0.54–i10.9) [30], the calculated complex refractive indices of the gold NP layer has a 10 times higher real part and a 10 times lower imaginary part. In other words, the layer behaves much less as a metal than as a dielectric. This is consistent with the size-dependent optical properties of thin gold films investigated in other papers [9–11,15], where the metallic character of gold is replaced with dielectric behavior with decreasing thickness, due to the confinement of free electrons caused by the interruption of percolation paths inside ultrathin metal films. Due to the electron mean free path of 25 nm [15], electrons are always confined in the gold NPs with an average thickness of 5.5 nm in the out-of-plane direction, suggesting dielectric-like optical properties for the TM-polarization. But the small-scale coalescence of

#225262 - $15.00 USD Received 20 Oct 2014; revised 3 Dec 2014; accepted 4 Dec 2014; published 15 Dec 2014

the aggregated gold NPs with average lateral size of 28 nm weakens the localization effect of electrons in the in-plane direction, which results in the more metallic complex refractive index of the gold NPs film for the TE-polarization (lower real part and higher imaginary part). For quantitative comparisons, the measured real parts of the complex permittivities (n^2-k^2) of the 5.3 nm and 6.2 nm thick gold evaporated films were around 25 and 10 at 1570 nm (0.79 eV) in air [3], respectively. From Figs. 5(c) and 5(d), the corresponding real parts of the anisotropic complex permittivities of the 5.5 nm gold film in air are 22.8 and 15 for the TM and TE polarizations, respectively, which are included within the above reported values. Moreover, the estimated complex refractive indices of the gold evaporated films with "nominal" thicknesses of 4 nm and 5 nm were found to be about 5-i1.5 and 4.5–i2.5 at 1570 nm in air [10], i.e. a similar real part as the one obtained here, but a much larger imaginary part. The origin of this discrepancy is that the gold films reported in [10] had larger-scale coalescence of the aggregated gold NPs than ours, which allowed more absorptive loss by Joule heating. The more connected gold films with lower thicknesses in [10] are probably caused by the difference between the mass-equivalent thickness and the effective thickness of the discontinuous gold films, which are correlated with each other by the filling factor (i.e. the mass-equivalent thickness of our gold NP film could be ~3.7 nm (5.5 × 68%)) [3,31]. Moreover, previous work on thin gold films (4-8 nm) used a quasi-homogeneous isotropic effective medium material for investigating their optical properties in visible and infrared wavelength regions [10,15]. Here we provide further observations of the anisotropy of these films and demonstrate that directional depolarization effect in oblate gold NPs [11,13,24] and the resulting anisotropic permittivity of ultrathin gold material [32,33], yields a measurable optical birefringence and dichroism.

For further investigating the anisotropic optical properties of the gold NPs coating under various SRIs, we now compare our measured results with theoretical calculations of the complex permittivity of an effective medium layer composed of gold NPs (using the bulk complex permittivity of gold at these wavelengths) and surrounding media. Two effective medium approximations (EMA) will be used, one based on the generalized M-G formula [34] and the other on the generalized Bruggeman formula [35]. From the SEM and AFM images shown in Fig. 2, the gold NPs can be represented as oblate gold spheroids embedded in the surrounding medium, where the minor axes of all oblate spheroids are perpendicular to the optical fiber surface. Thus, the generalized M-G and Bruggeman formulas can be respectively expressed as [34,35],

$$\frac{\varepsilon_{eff}-\varepsilon_e}{\varepsilon_e+N_{TM,TE}(\varepsilon_{eff}-\varepsilon_e)}=f\frac{\varepsilon_i-\varepsilon_e}{\varepsilon_e+N_{TM,TE}(\varepsilon_i-\varepsilon_e)} \tag{3}$$

$$(1-f)\frac{\varepsilon_{eff}-\varepsilon_e}{\varepsilon_{eff}+N_{TM,TE}(\varepsilon_e-\varepsilon_{eff})}=f\frac{\varepsilon_i-\varepsilon_{eff}}{\varepsilon_{eff}+N_{TM,TE}(\varepsilon_i-\varepsilon_{eff})} \tag{4}$$

where ε_{eff} is the effective permittivity of the effective medium layer, ε_i and ε_e are the permittivities of inclusion (gold) and surroundings, respectively, $N_{TM,TE}$ is the depolarization factor for TM or TE-polarization, and f is the volume factor of the gold material. For the oblate gold spheroids, the depolarization factors of the TM- and TE-polarizations can be defined as a function of the aspect ratio x of the oblate spheroid [36],

$$N_{TM}=(1+1.6x+0.4x^2)^{-1} \tag{5}$$

$$N_{TE}=(1-N_{TM})/2 \tag{6}$$

where N_{TM} and N_{TE} are 0.752 and 0.124 for our structure, based on the following expression for $x=h_{NP}/d_{NP}$. With Eqs. (3) and (4), the calculated complex refractive indices of the

#225262 - $15.00 USD Received 20 Oct 2014; revised 3 Dec 2014; accepted 4 Dec 2014; published 15 Dec 2014

effective medium coating under the three SRIs for the out-of-plane (TM) and in-plane (TE) directions are shown in Fig. 6, where the corresponding results obtained from the experimental data are also indicated.

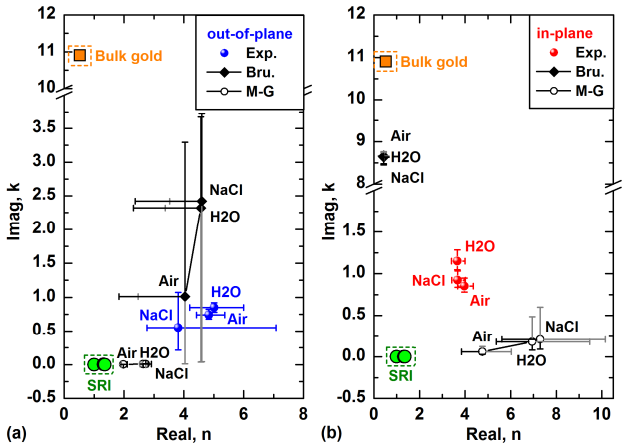

Fig. 6. Complex refractive indices of the effective medium coating of the three surroundings for (a) out-of-plane (TM) and (b) in-plane (TE) directions calculated by M-G and Bruggeman EMAs, compared with the experimentally obtained results and the bulk permittivities of the medium constituents (gold and SRI). The gray and black error bars indicate the deviations of complex refractive indices caused by the minimum aspect ratio x of 4.5/36 and the maximum x of 6.5/20 in EMA models, respectively, based on the average height of 5.5 nm (± 1 nm) and the average lateral dimensions of 28 nm (± 8 nm) of the gold NPs. Note that the both of gray and black error bars show in negative direction for the real parts of Bruggeman EMA in Fig. 6(a).

Based on these comparisons of the three groups of complex refractive indices, some general trends can be observed. As expected from the EMA of metal particles in dielectric media, the large increase in the real part of the index of the film relative to that of its constituents is relatively well modeled, with the notable exception of the Bruggeman model for the in-plane (TE) polarization. In this latter case the model predicts a complex index that is very close to that of bulk gold (regardless of SRI), while the experimental data retains a strong dielectric behavior. It is as if the EMA layer was acting as a continuous metal barrier for light in the cladding and shielding it completely from the surroundings, which is not the case according to the experimental data but which does occur for thicker films [19]. The other observation is that the M-G EMA systematically underestimates the coating loss (k), as expected in this case [37], while the Bruggeman model does the opposite (overestimates). An underestimated EMA value for loss is expected because the experimental values for loss come from two contributions in our experiments: absorption by gold NPs and scattering of the evanescent fields of cladding guided modes. Since the EMA approach does not include the effect of scattering, it was expected that those models would underestimate k relative to the experiments. It is clearly not the case for the Bruggeman EMA which again reflects its tendency to overestimate the loss due to absorption (i.e. the metallic character of the ultrathin coating with such aspect ratio of its constituent NPs). In fact, the applicability of the various EMAs to the different steps of growing gold NPs film deposited on glass that was described in [38] indicates that the M-G formula is quite suitable for sparsely distributed gold NP films while the Bruggeman formula is applicable when there is large-scale coalescence in the gold film growth. It looks from the results presented here that for intermediate levels of coalescence of ultrathin gold NP films, both EMA formulas fail in reproducing the experimental data. Some similar failures of the Bruggeman EMA were also observed in fitting the measured complex conductivities (directly related to complex permittivity) and optical transmittance at far-infrared frequency for gold films around the insulator-to-metal transition

#225262 - $15.00 USD Received 20 Oct 2014; revised 3 Dec 2014; accepted 4 Dec 2014; published 15 Dec 2014

[39,40]. Our results for the anisotropic complex refractive index show that this gold NP film at a thickness of 5.5 nm is thicker than the critical value for the maximum dielectric constant, in agreement with measured critical thicknesses between 5.3 nm and 6.2 nm for light at a wavelength of 1570 nm (0.79 eV) [3]. The slightly weaker insulating properties of the gold NPs film for the in-plane polarization (TE) are understandable since the dipole coupling between the gold NPs should occur first for in-plane polarization and help the gold film tend toward metallic material as the film grows [11]. However, the significant differences in the birefringence and absolute values of the measured effective medium results as a function of SRI are unexpected and may reveal new and important effects that occur near the insulator-to-metal transition of gold at these thicknesses and wavelengths.

5. Conclusion

In conclusion, the SRI-dependent effective refractive indices of the anisotropic 5.5 nm gold NPs film deposited by gold evaporation method were investigated with the polarized cladding modes excited by a TFBG. The complex refractive indices for modes polarized in the in-plane (TE) and out-of-plane (TM) directions, and the corresponding effective thin coating parameters were extracted from the measured polarization-dependent wavelength shifts and amplitude changes of the cladding modes around 1570 nm with help from simulations carried out with an accurate four-layer complex mode solver. For the extracted complex refractive indices of the gold NPs film embedded in different media, the results show that the real parts are 10 times larger than for bulk gold while the imaginary parts of the film are 10 times smaller. Such ultrathin gold films with only small scale coalescence have therefore a strong dielectric nature. It is worth noting that for the gold NP sizes obtained here, the localized surface plasmon resonance (LSPR) wavelength is near 750 nm, i.e. well outside of our measurement spectral range. While some of the NPs have larger sizes and hence longer LSPR wavelengths, the randomness of the sizes would smear out any significant impact. Therefore no plasmonic effect is expected to come into play. The slightly weaker insulating optical properties of the gold NPs film for the TE-polarization than those for TM-polarization suggest the proximity of an insulator-to-metal transition and a critical thickness lower than 5.5 nm at 1570 nm, for the deposition conditions used. Moreover, comparing the experimental results with predictions from the generalized M-G and Bruggeman EMAs, it was revealed that these effective medium models fail to correctly account for the properties of the NP films at such thickness for near infrared wavelengths. The EMA models also do not correctly account for the effect of augmenting the surrounding medium permittivity on the birefringence and dichroism of the gold NPs film. In view of the increasing importance of thin metal coatings in plasmon-assisted sensing and in photovoltaic devices, the polarization-resolved, high sensitivity measurements reported here show that ultrathin, partially connected metal films have anisotropic effective complex permittivities that are not well modelled by currently accepted EMA theories that are based on bulk metal properties with shape and density factors alone. It was also demonstrated clearly that the evolution of the equivalent film properties with SRI presents some anomalous features that are not consistent with our understanding of the effect of thin perturbations on guided modes, especially in the important case of saline solutions.

Acknowledgments

This work is supported by the Natural Science and Engineering Research Council of Canada, the Canada Foundation for Innovation, and the Canada Research Chairs program. WZ would like to acknowledge Ms. Angela McCormick for cleaning optical fibers and operating gold physical vapor deposition. DJM would like to acknowledge the Centre for Catalysis and Research Innovation (CCRI) at the University of Ottawa for use of SEM and AFM.